

Article

# Facile Synthesis, Characterization, and Photocatalytic Activity of Hydrothermally Grown Cu<sup>2+</sup>-Doped ZnO–SnS Nanocomposites for MB Dye Degradation

Govinda Dharmana<sup>1</sup>, Thirumala Rao Gurugubelli<sup>1</sup> , Prabhakara Srinivasa Rao Masabattula<sup>1,\*</sup>,  
Bathula Babu<sup>2,\*</sup>  and Kisoo Yoo<sup>2,\*</sup>

<sup>1</sup> Physics Division, Department of Basic Sciences and Humanities, GMR Institute of Technology, Rajam 532127, Andhra Pradesh, India; govind6687@gmail.com (G.D.); thirumala.phy@gmail.com (T.R.G.)

<sup>2</sup> School of Mechanical Engineering, Yeungnam University, Gyeongsan 712-749, Korea

\* Correspondence: mpsr@rediffmail.com (P.S.R.M.); babu.physicist@gmail.com (B.B.); kisooyoo@yu.ac.kr (K.Y.)

**Abstract:** The morphology, chemical composition, and doping process of metal oxides and sulfides play a significant role in their photocatalytic performance under solar light illumination. We synthesized Cu<sup>2+</sup>-doped ZnO–SnS nanocomposites at 220 °C for 10 h, using hydrothermal methods. These nanocomposites were structurally, morphologically, and optically characterized using various techniques, including powder X-ray diffraction (XRD), transmission electron microscopy (TEM), X-ray photoelectron spectroscopy (XPS), and UV-visible absorption spectroscopy. Their photocatalytic activity (PCA) on methylene blue (MB) pollutant dye was examined under 150 W solar light illumination. Mixed-phase abundances with hexagonal ZnO and orthorhombic SnS structures were observed. TEM micrographs showed changes in morphology from spherical to nano-flake structures with an increasing doping concentration. XPS indicated the chemical states of the constituent elements in the nanocomposites. UV-visible absorption spectroscopy showed a decrease in the bandgap with an increasing doping concentration. Strong PCA was observed due to the separation of charge carriers, a change in bandgap, and a high light absorption ability under solar light irradiation. The measured photodegradation efficiency of the MB dye was approximately 97% after 2 h. The movement of the charge carriers and the bandgap alignment of the synthesized composites are briefly discussed.

**Keywords:** Cu<sup>2+</sup>-doped ZnO–SnS; hydrothermal; photocatalysis; methylene blue



**Citation:** Dharmana, G.; Gurugubelli, T.R.; Masabattula, P.S.R.; Babu, B.; Yoo, K. Facile Synthesis, Characterization, and Photocatalytic Activity of Hydrothermally Grown Cu<sup>2+</sup>-Doped ZnO–SnS Nanocomposites for MB Dye Degradation. *Catalysts* **2022**, *12*, 328. <https://doi.org/10.3390/catal12030328>

Academic Editors: Ioannis Konstantinou and Vincenzo Vaiano

Received: 2 February 2022

Accepted: 10 March 2022

Published: 13 March 2022

**Publisher's Note:** MDPI stays neutral with regard to jurisdictional claims in published maps and institutional affiliations.



**Copyright:** © 2022 by the authors. Licensee MDPI, Basel, Switzerland. This article is an open access article distributed under the terms and conditions of the Creative Commons Attribution (CC BY) license (<https://creativecommons.org/licenses/by/4.0/>).

## 1. Introduction

Environmental pollution has reached unacceptable levels due to the rapid growth of civilization and industrialization. Water resources are contaminated by effluents released from industries, such as oil refineries and cement, textiles, pulp, and paper plants. Organic dyes (pigments) and various types of herbicides (for example 2, 4-D, and 2,4-DCP) pollute freshwater bodies [1,2]. These pigments reduce the quality of water in terms of pH and pose a high risk to people and aquatic life. Therefore, the reduction of the toxicity levels of organic dyes such as methyl orange (MO), ciprofloxacin (CIP), methylene blue (MB), acid orange (AO), and rhodamine B (RhB) in freshwater bodies is crucial [3]. The current research priority is finding environmentally friendly and easily implementable methods for the removal of organic pollutants. Most organic dyes and other toxic industrial pollutants in water bodies can be removed using strategies [4] such as photocatalysis, reverse osmosis, and chemical and biological methods. Photocatalysis plays a vital role in the degradation of pigments in water bodies. Other advanced oxidation processes [5] such as ozonation and Fenton and non-thermal plasma processes also degrade organic contaminants such as MB. Semiconductor-mediated photocatalysis has gained attention due to its simple conditions, renewable energy production, environmental safety, high output, uniform production, maximized pigment removal, and low energy consumption [6]. Photocatalytic degradation

using visible or ultraviolet (UV) light as the source of illumination is considered an important method of water purification. It can produce total mineralization of pigments in water and extract them without leaving detrimental residues and has become an indispensable technology. Oxide semiconductor nanostructures with small dimensions exhibit quantum confinement effects and have shown great promise in resolving challenges related to energy and the environment. Oxide semiconductors are also widely used in solar light-harvesting and high-efficiency photoexcitation devices [7].

In the present study, a ZnO n-type direct bandgap semiconductor was selected as a promising material for achieving high photocatalytic activity. ZnO has attracted widespread research interest owing to its important characteristics such as wide bandgap (3.37 eV), nontoxicity, abundance in nature, thermal and chemical stability, low cost, transparency, high excitation energy, and high electron mobility [8]. Furthermore, ZnO is widely used in several practical applications such as optoelectronic devices, biosensors, biomedical applications, photocatalytic materials, and photonics. However, applications of ZnO in photocatalysis are restricted because of the rapid formation of excitons in addition to a partial response to visible light [9]. To overcome this drawback and enhance the photocatalytic efficiency of oxide semiconductors with high absorption in the solar region, it is imperative to merge them with suitable photosensitized materials. Mid- or narrow-bandgap materials are used to absorb large amounts of solar light by incorporating doped metal nanoparticles, Z-scheme mechanisms, nanocrystals, and inorganic semiconducting materials. We targeted the versatile p-type narrow bandgap (1.3–1.5 eV) semiconductor SnS as a sensitizer material. This forms a novel ZnO–SnS (n-p type) heterojunction, which can serve as an efficient photocatalyst to improve the degradation of organic pollutants in freshwater bodies [10]. SnS was chosen because it is highly abundant, non-toxic, and environmentally safe. It behaves as an active photocatalyst under visible light irradiation with high absorption capacity. Thus, a ZnO–SnS heterojunction should exhibit enhanced absorption of solar energy and induce the separation of photogenerated charge carriers on the surface of the photocatalyst, thus achieving maximum photocatalytic performance [11]. Although the performance of heterojunction nanocomposites in the degradation of water pollutants is adequate, their low generation rate of electron-hole pairs limits their photocatalytic efficiency [12]. To overcome this problem, doping of transition and rare earth metal ions and graphene-based compounds into the host lattice has recently been introduced. Transition metal [Cu, Mn, Fe, V, Ni, Pt, Ag, Pd, and Cr] ions have shown great potential. These ions improve the structural, optical, and magnetic properties of heterojunction nanocomposites and play a critical role in determining their superior photocatalytic activity under UV-visible light illumination [13]. Further, doping in oxide semiconductors causes the creation of new acceptor and donor energy levels usually located in the region between the valence (VB) and the conduction bands (CB) in the co-catalyst material.

Recent studies have revealed that composite nanostructures exhibit superior photocatalytic activity compared to individual nanostructures. Wang et al. reported the synthesis of a SnNb<sub>2</sub>O<sub>6</sub>–ZnO nanocomposite by a hydrothermal method. This achieved photodegradation efficiencies of 95% in 60 min of RhB dye and of 96% in 120 min of phenol [14]. Xu et al. synthesized a ZnO-decorated SnO<sub>2</sub> nanopowder by hydrothermal means. They reported that the particle size of the ZnO–SnO<sub>2</sub> composite was smaller than that of pure ZnO and SnO<sub>2</sub>, and the photocatalytic activity of the composite was superior to that of pure SnO<sub>2</sub> [15]. Xu et al. demonstrated that ZnO–SnO<sub>2</sub> hierarchical nanostructures, synthesized by a simple two-step microwave-assisted hydrothermal process, resulted in an effective photocatalytic degradation performance of 97.9% on MB dye [16]. Gurugubelli et al. reported enhanced photocatalytic performance of ZnO–CdS nanocomposites in the degradation of RhB dye under solar light and found that the composite nanostructures exhibited superior degradation efficiency compared to bare ZnO and CdS nanoparticles [17]. Makama et al. reported the microwave pulse-assisted synthesis of ZnO–SnS<sub>2</sub> nanocomposites for the degradation of MB dye under solar light, with 98.2% degradation efficiency [18]. To the best of our knowledge, there are no reports on the influence of Cu<sup>2+</sup> ions on ZnO–SnS nanocomposites.

In this study,  $\text{Cu}^{2+}$  ions were incorporated into ZnO–SnS nanocomposites to obtain superior photocatalytic activity under solar light irradiation.  $\text{Cu}^{2+}$  ions were selected as dopants because of their high thermal and electrical conductivity, physical and chemical properties that closely resemble Zn, large ionization energy, rapid incorporation into the host lattice, high photocatalytic efficiency, and isomorphic nature [19]. Among the existing fabrication methods, the hydrothermal method is preferred for the preparation of nano-phased materials at high temperature (up to 300 °C) and pressure (up to 10 bar) conditions [20]. The hydrothermal method has the advantages of uniform production, facile conditions, environmental safety, and low output loss. Further, the reaction process can be controlled by the vapor pressure and yield of unstable particles at higher temperatures. MB (formula  $\text{C}_{16}\text{H}_{18}\text{ClN}_3\text{S}$ , molecular weight 319.852 g/mol, wavelength 664 nm, and color index 52.015) was selected [21] as a model pollutant for the study of the photocatalytic activity of  $\text{Cu}^{2+}$ -doped ZnO–SnS nanocomposites under solar light irradiation.

## 2. Results and Discussion

### 2.1. X-ray Diffraction Study

XRD was the preferred technique to determine the structural properties and phase identification of the synthesized samples. The XRD patterns of undoped ZS and  $\text{Cu}^{2+}$ -doped ZS (ZS-C1, ZS-C3, and ZS-C5) samples are shown in Figure 1. The XRD peaks indicate the mixed-phases abundance of wurtzite hexagonal ZnO and orthorhombic SnS structures. The diffraction planes (002), (101), (102), (110), (103), and (202) indicate the hexagonal phase of ZnO, according to the Joint Committee on Powder Diffraction Standards (JCPDS) pattern 36-1451, shown at the bottom of Figure 1. Similarly, the lattice planes (120), (111), (131), (112), (042), (212), and (311) confirmed the orthorhombic phase of SnS, shown in JCPDS 39-0354. Further, the peak intensity in the (111) plane is higher than that of the other peaks, inferring a favorable accommodation of nanocomposite formation [22]. No additional impurity peaks related to the doping element (Cu) were observed. The average crystallite size ( $D$ ) of the prepared nanocomposites was calculated using Scherrer's equation [23]:

$$D = \frac{0.9 \lambda}{\beta \cos \theta} \quad (1)$$

where  $\lambda$  is the Cu-K $\alpha$  radiation wavelength,  $\beta$  is the full width at half maximum (FWHM), and  $\theta$  is the angle of diffraction.

The microstrain ( $\epsilon$ ) and the dislocation density ( $\delta$ ) of each sample were evaluated using the expressions [24]:

$$\epsilon = (\beta \cos \theta) / 4 \text{ and } \delta = 1 / D^2 \quad (2)$$

The estimated average crystallite size,  $d$ -spacing, microstrain, and dislocation density values for the undoped and  $\text{Cu}^{2+}$ -doped ZS nanocomposites are presented in Table 1. These results showed that particle size and  $d$ -spacing decreased with an increasing doping content in the ZS nanocomposites.

**Table 1.** Average crystallite size,  $d$ -spacing, microstrain, and dislocation density of undoped and  $\text{Cu}^{2+}$ -doped ZnO–SnS nanocomposites.

Sample	Crystallite Size (D nm)	$d$ -Spacing (Å)	Microstrain ( $\epsilon$ ) $\times 10^{-3}$	Dislocation Density ( $\delta$ ) $\times 10^{15}$ Lines/m <sup>2</sup>
ZS	7.9	2.61	5.33	1.60
ZS-C1	7.4	2.45	5.11	1.82
ZS-C3	6.8	1.88	4.65	2.16
ZS-C5	6.5	1.61	4.38	2.33

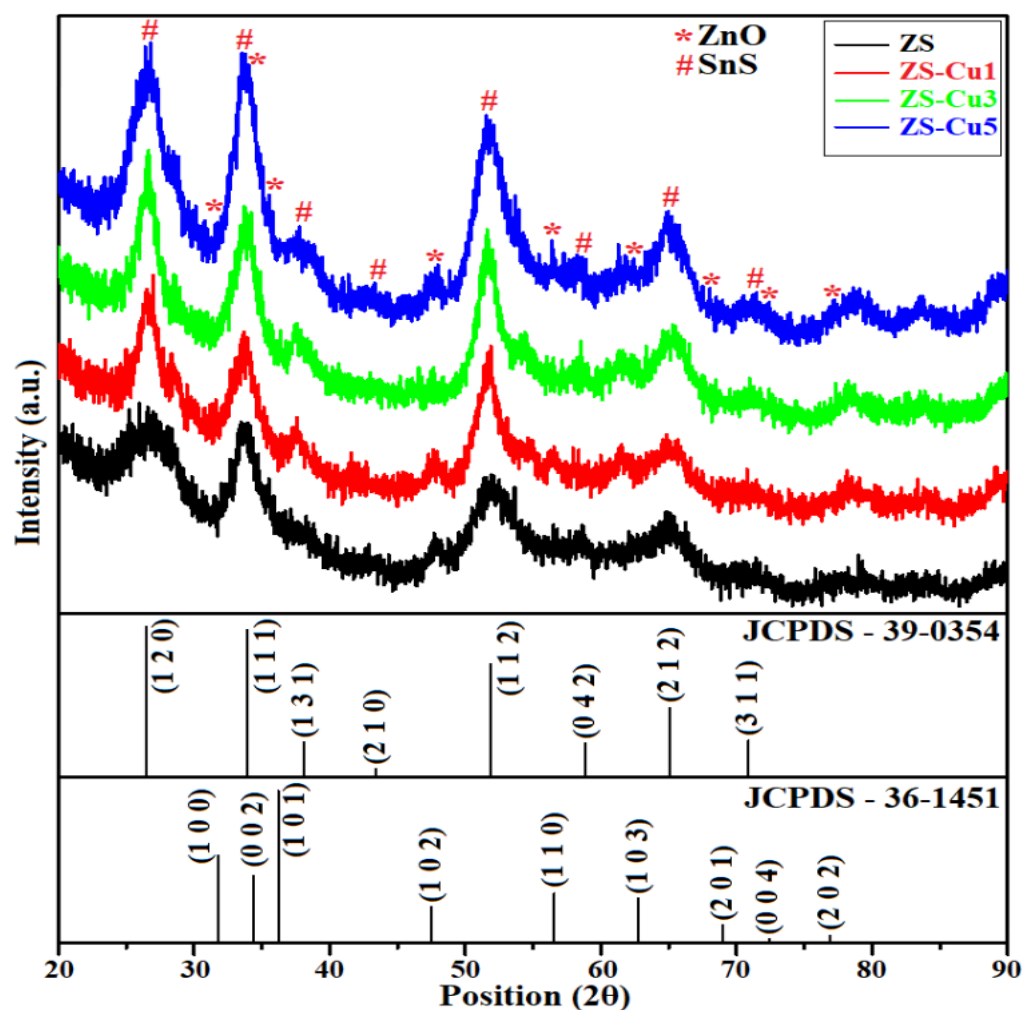
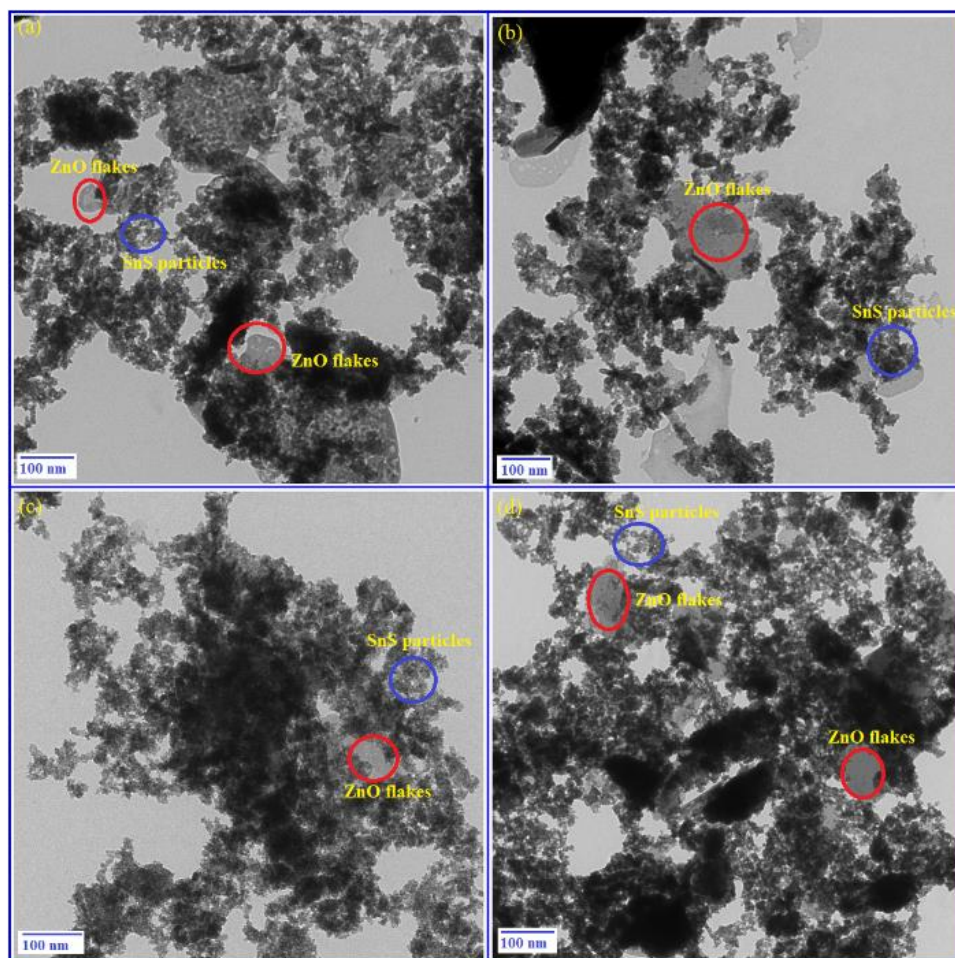


Figure 1. X-ray diffraction patterns of undoped and Cu<sup>2+</sup>-doped ZnO–SnS nanocomposites.

## 2.2. Morphological Study

TEM was used to observe the crystal growth, analyze the microstructures, and determine the morphological properties [25] of the samples. Figure 2 shows the TEM micrographs of the undoped and Cu<sup>2+</sup>-doped ZS nanocomposites. Undoped ZS, shown in Figure 2a, exhibited mostly nanoflake and polygon-like structures. However, with increasing Cu<sup>2+</sup> doping (Figure 3b–d), the morphology changed. This modification in morphology implies a change in the inter-atomic distance between ZnO and Cu<sup>2+</sup> ions, which affected the high surface area and crystal growth of the nanoparticles. The presence of Cu<sup>2+</sup> ions accelerated the ZnO lattice structure and exhibited some agglomeration, which increased with an increasing doping (Cu<sup>2+</sup>) concentration. Figure 2b, with doping content of 1%, reveals an uneven distribution of the SnS nanoparticles on the surface of the ZnO nanoflakes. A further increase in the Cu<sup>2+</sup> content to 3% (Figure 2c) revealed a uniform distribution of the SnS nanoparticles on ZnO surface. A further increase in the doping content to 5% resulted in more agglomerates, as shown in Figure 2d. The agglomeration might be due to the interaction of the nanoparticles and large nanoflakes with the Cu<sup>2+</sup> ions heavily accumulated in the ZS nanocomposite [26].



**Figure 2.** TEM images of (a) ZS, (b) ZS-C1, (c) ZS-C3, and (d) ZS-C5 nanocomposites.

### 2.3. XPS Study

XPS was used for elemental analysis and for determining the chemical state of each synthesized sample. We also needed to find the particle surfaces and constituent elements of the nanocomposites. The binding energies of all the elements (Zn, O, Sn, S, and Cu) in the prepared nanocomposites are presented in the high-resolution survey scan spectrum (0 to 1300 eV) shown in Figure 3a. Other elements detected were C and N due to instrument/environment effects and O<sub>2</sub> due to adsorption. The XPS analysis of the dopant element (Cu), depicted in Figure 3b, showed prominent characteristic peaks at binding energies of 932.59 eV and 953.41 eV, ascribed to Cu 2p<sub>3/2</sub> and Cu 2p<sub>1/2</sub> states. These confirmed the existence of Cu in the Cu<sup>2+</sup> oxidation state, with a spin-orbit splitting value of 20.82 eV [27]. The high-resolution XPS spectrum of Zn presented in Figure 3c shows two remarkable peaks at binding energies 1021.92 eV and 1044.98 eV, ascribed to the Zn 2p<sub>3/2</sub> and Zn 2p<sub>1/2</sub> states of Zn<sup>2+</sup>, with a characteristic spin-orbit splitting value of 23.06 eV [28]. The O XPS spectrum (Figure 3d) shows the presence of clear O 1s peaks at 530.21 eV and 531.69 eV. These were ascribed to the formation of core-level lattice structures of oxygen anions in the O<sup>2-</sup> oxidation state and the adsorption of water, respectively [14]. The core-level XPS spectrum of Sn is shown in Figure 3e. A significant peak was detected at binding energy 486.35 eV, along with a satellite peak at binding energy 494.76 eV. These were ascribed to the Sn 3d<sub>5/2</sub> and Sn 3d<sub>3/2</sub> states of Sn<sup>2+</sup>, with the spin-orbit splitting value of 8.41 eV [29]. The S XPS spectrum in Figure 3f is turbulent, with a strong peak at binding energy 163.24 eV and a satellite peak at 164.55 eV. These peaks confirmed the existence of the S 2p<sub>3/2</sub> and S 2p<sub>1/2</sub> states. They were attributed to the fixing of the S<sup>2-</sup> oxidation state, with a spin-orbit splitting value of 1.35 eV [30]. The electronic interaction

between the metal nanoparticles and the metal oxide was responsible for the shifting of the XPS peaks towards lower binding energy levels. A reduction in electron density generally leads to a higher binding energy; as a result, a limited number of electrons are transferred from ZnO to SnS to construct an effective ZnO–SnS heterojunction with a proper doping element concentration. Thus, the XPS study successfully examined the chemical states of all constituent elements in the prepared samples, including  $\text{Cu}^{2+}$  doping.

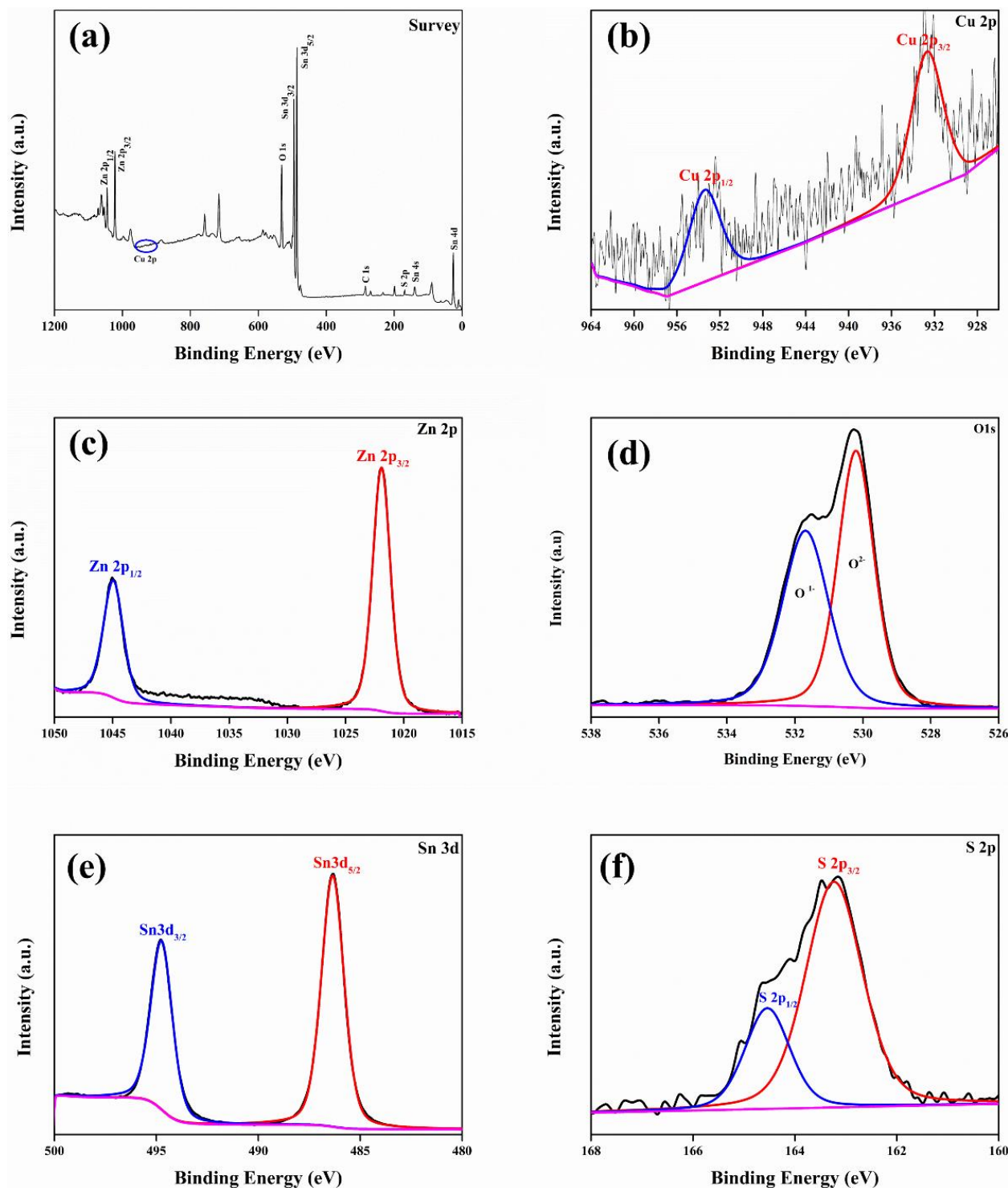
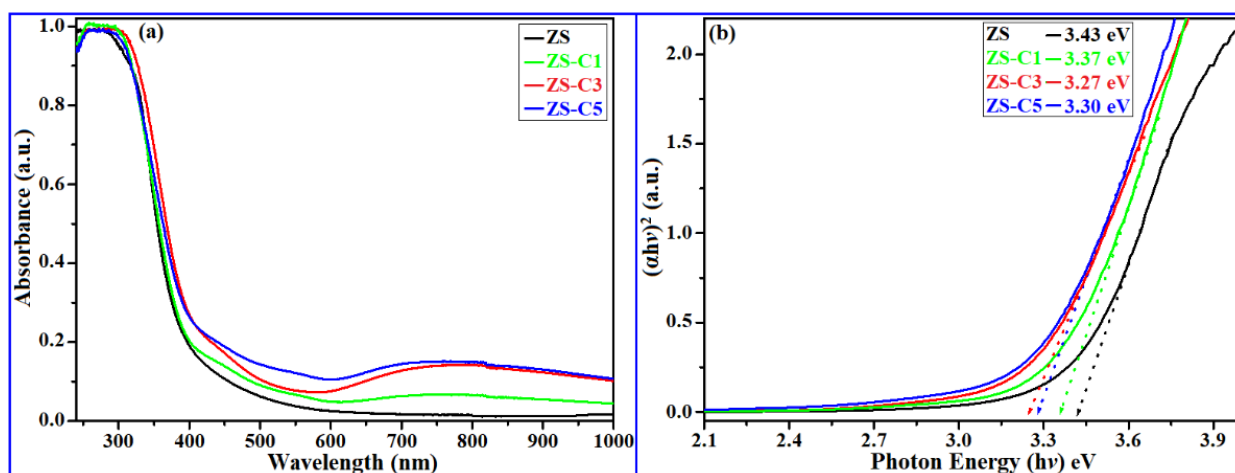


Figure 3. XPS spectra of Cu<sup>2+</sup>-doped (3%) ZnO–SnS (ZS-C3) nanocomposite: (a) survey, (b) Cu 2p, (c) Zn 2p, (d) O 1s, (e) Sn 3d, and (f) S sp.

#### 2.4. Absorption Study

UV-visible DRS [31] was used to analyze the energy bandgaps ( $E_g$ ) and optical properties of the nanocomposites. The optical absorption spectra of the undoped and  $\text{Cu}^{2+}$ -doped ZS samples are shown in Figure 4a. The energy bandgaps were derived using Tauc plots, as shown in Figure 4b. The optical bandgap of the synthesized samples was calculated using the Tauc relation [32],

$$\alpha h\nu = a(h\nu - E_g)^m \quad (3)$$



**Figure 4.** (a) Optical absorption and (b) Tauc plots of undoped and  $\text{Cu}^{2+}$ -doped ZnO–SnS nanocomposites.

The energy bandgap values for the ZS, ZS-C1, ZS-C3, and ZS-C5 samples were found to be 3.43 eV, 3.37 eV, 3.27 eV, and 3.30 eV, respectively. This indicated that as the  $\text{Cu}^{2+}$  doping concentration increased in the ZS host nanocomposites, the energy bandgap decreased significantly, owing to defects/vacancies related to O. Of all the synthesized samples, ZS-C3 had the lowest energy bandgap of 3.27 eV. This was probably due to a uniform dispersion of the  $\text{Cu}^{2+}$  ions on the surface of the ZS host nanocomposite matrix. A tunable bandgap energy is highly favorable for superior photocatalytic activity in the solar region [33]. Thus, we consider the ZS-C3 photocatalyst to be the best optimized sample.

#### 2.5. Photocatalytic Activity

The detoxification of organic pollutants such as MB in water bodies polluted by industrial effluent is necessary to protect the health of people and aquatic environments. Our study aimed to degrade the MB dye in wastewater by achieving a good photocatalytic behavior under 150 W solar light irradiation. Figure 5 depicts the nature of the photocatalytic activity (PCA) of undoped and  $\text{Cu}^{2+}$ -doped ZS nanocomposites. The PCA of the synthesized samples was examined in aqueous solution irradiated with solar light at ambient temperature. The concentration of degraded MB was examined using an absorption spectrophotometer every 15 min over a period of 120 min. First, a ‘blank experiment’ was performed [34] using pure MB in aqueous solution to determine the stability and degradation efficiency of the dye under solar light illumination. However, aqueous solutions of the dye only show very little degradation under solar light. To achieve significant degradation, nano photocatalyst materials (ZS-C composites) must be added. Each sample was magnetically stirred in the dark, ensuring the photocatalyst material would uniformly affect the dye degradation process, leading to a saturated adsorption equilibrium. It was observed that the  $\text{Cu}^{2+}$ -doped nanocomposites (ZS-C1, ZS-C3, and ZS-C5) exhibited superior PCA compared to the ZS (host) nanocomposite. This enhancement in efficiency was attributed to changes in the energy bandgap of the ZS composite by  $\text{Cu}^{2+}$  doping. New energy levels were introduced within the bandgap region, and this promoted robust photocatalytic activity in solar light sensitization [35]. The impact of  $\text{Cu}^{2+}$  doping on the

photocatalytic performance of the ZS composites under solar light illumination is depicted in Figure 5a. The order of increasing MB dye degradation efficiency of the samples was ZS < ZS-C1 < ZS-C5 < ZS-C3. The photocatalytic degradation efficiency was evaluated in terms of the Langmuir-Hinshelwood model. In this model, the concentration of the degrading material decreases with time according to [36]

$$C_t = C_0 \exp(-kt) \quad (4)$$

where  $C_0$  is the initial concentration,  $C_t$  is the concentration after the time interval  $t$  in min, and  $k$  is the kinetic rate constant in  $\text{min}^{-1}$ . Alternatively,  $k$  is defined by the first-order pseudo-kinetic Langmuir-Hinshelwood relation [36]:

$$k = \frac{\ln(C_0/C_t)}{t} \quad (5)$$

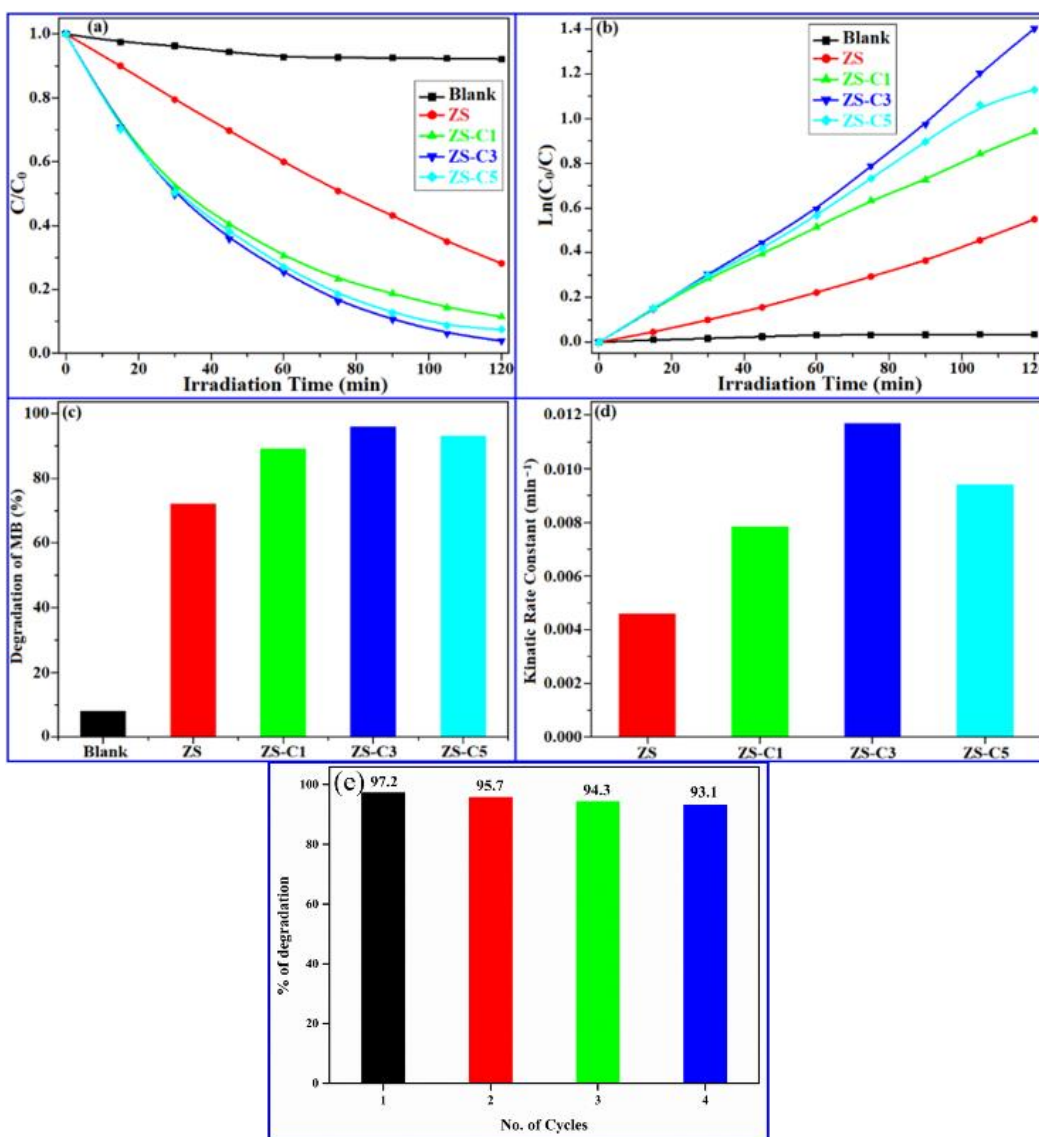


**Figure 5.** Photocatalytic activity of undoped and  $\text{Cu}^{2+}$ -doped ZnO-SnS nanocomposites: (a) concentration, (b) kinetics for the MB dye, (c) degradation efficiency, (d) kinetic rate constants of the catalysts, and (e) reusability test of ZS-C3 under solar light illumination.

Figure 5b shows a graph of  $\ln(C_0/C_t)$  versus illumination time  $t$ . It is a straight line, indicating that the photodegradation process obeyed the first-order Equation (5). The photodegradation efficiencies of our photocatalyst composites in MB dye aqueous solutions for a solar light irradiation time of 120 min are shown in Figure 5c. The degradation percentages were 11.4%, 71.7%, 87.8%, 97.2%, and 92.6% for blank, ZS, ZS-C1, ZS-C3, and ZS-C5, respectively. Of the prepared nanocomposites, the ZS-C3 (optimized sample) photocatalyst showed the highest PCA of 97.2% over 120 min, which was attributed to the nature of the energy bandgap and to plasmonic effects. Owing to the high radiative recombination rate of photogenerated charge carrier ( $e^-$ - $h^+$ ) pairs on its surface, the undoped ZS photocatalyst degraded only 71.7% of the MB dye. The values of the kinetic rate constant obtained using Equation (5) for the synthesized composites ZS, ZS-C1, ZS-C3, and ZS-C5 were  $0.0039 \text{ min}^{-1}$ ,  $0.0071 \text{ min}^{-1}$ ,  $0.0121 \text{ min}^{-1}$ , and  $0.0089 \text{ min}^{-1}$ , respectively. The ZS-C3 optimized sample displayed the highest kinetic rate constant among all samples, corresponding to maximum MB dye removal under solar light irradiation.

Figure 5d shows a bar diagram comparing the kinetic rate constants of the synthesized composites. It is clearly observed that  $\text{Cu}^{2+}$ -doped nanocomposites (ZS-C1, ZS-C3, and ZS-C5) exhibited improved photodegradation efficiencies over the undoped ZS host composite, because of the assimilation of copper ions into the ZS lattice structure. In addition,  $\text{Cu}^{2+}$  doping introduced new energy levels within the bandgap limits in the region of the conduction band of the ZS lattice. The doping ions thus effectively reduced the energy bandgap of the nanocomposites [37]. This narrow band gap facilitated the separation of photogenerated charge carriers (recombination of fewer electron-hole pairs) on the surface of the photocatalyst, so that  $\text{Cu}^{2+}$ -doped novel heterojunction nanocomposites (ZS-C) exhibited superior PCA under solar light irradiation. It was also observed that the photodegradation efficiency of copper-doped ZS nanocomposites tended to increase with an increasing copper content. However, the maximum photodegradation efficiency was obtained for the ZS-C3 (3%) catalyst, and the efficiency decreased for the ZS-C5 (5%) catalyst. In the case of ZS-C5, the incidental agglomeration of  $\text{Cu}^{2+}$  ions into ZS host lattice sites tended to reduce the bandgap and caused the scattering of light. The photodegradation efficiencies of the nanocomposites with respect to MB are compared in Table 2. This shows the ZS-C3 catalyst material exhibited the highest photodegradation efficiency, that is, maximum PCA, and induced large numbers of self-activation centers on the surface of these optimized nanocomposites. Moreover, doping ions ( $\text{Cu}^{2+}$ ) created new energy levels in the region of the CB and VB of the Z-S host lattice structure, leading to a tunable bandgap in the nanocomposites. We conclude that  $\text{Cu}^{2+}$ -doped ZS nanocomposites exhibit high absorption of light and robust PCA under solar light irradiation. Moreover, our photocatalyst composites have advantages such as low cost, high absorption ability, reusability, environmental friendliness, and robust photocatalytic performance. It is anticipated that the optimized nanophotocatalyst material will be employed to remove organic contaminants from water bodies to the greatest extent possible. The superior photocatalytic degradation performance of the ZS-C3 optimized nanocomposite over others motivated reusability and stability tests on this sample for its use in a variety of practical applications.

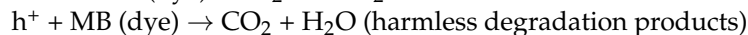
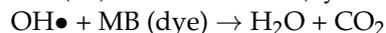
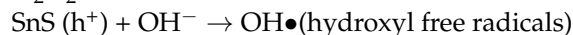
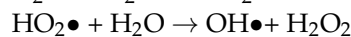
Figure 5e depicts the results of the reusability test on ZS-C3 for MB dye degradation under solar light illumination. The test results indicated that a slight decrease in the photodegradation percentage of MB dye was observed after four usage cycles. However, approximately 93% degradation remained after the complete recycling test. Our ZS-C3 optimized nano photocatalyst thereby clearly demonstrated its potential for reuse in practical decontamination applications.

**Table 2.** Comparison of the photocatalytic efficiencies of various ZnO-based nanocomposites in the degradation of methylene blue (MB).

Catalyst	Synthesis Method	Dye	Light Source	Irradiation Time (min)	Degradation Efficiency (%)	Ref.
PANI/ZnO	Sonication	MB	Visible	180	99	[38]
ZnO/PEDOT	Solid-state	MB	Sun light	300	95	[39]
Sn doped CeO <sub>2</sub> -Fe <sub>2</sub> O <sub>3</sub>	Thermal deposition	MB	Visible	120	~94.5	[40]
ZnO/PANI	Rapid mixing polymerization	MB	Visible	160	76	[41]
rGO/ZnO/Ag	Hydrothermal	MB	Sun light	60	94	[42]
PANI/ZnO	Chemical polymerization	MB	Sun light	300	99	[43]
Cu-doped ZnO/SnS	Hydrothermal	MB	Solar	120	97.2	Present work

### 2.6. Proposed Transport Mechanism

The nature of the photocatalyst bandgap and the degree of charge carrier separation on the nanocomposite surface may determine the photocatalytic transport mechanism. Based on the results of the present work, the proposed charge carrier transport mechanism of the Cu<sup>2+</sup>-doped ZS-optimized photocatalyst is depicted in Figure 6. Zn lattice sites are replaced by Cu<sup>2+</sup> ions; therefore, the tunable bandgap nature of the photocatalyst is solely controlled by the doping ions. The location of the Fermi energy ( $E_F$ ) level in the ZnO and SnS materials is shifted due to the impurity concentration, so that the CB of SnS lies just above the CB of the Cu<sup>2+</sup>-doped ZnO energy state, and the VB of SnS lies above the VB of Cu<sup>2+</sup>-doped ZnO energy level [11]. Thus, our novel heterogeneous ZnO–Cu/SnS structure with a ZnO–SnS interface can act as a possible medium for the transformation of photogenerated charge carriers on the surface of the nanocomposite through allowed self-activated lattice sites [44]. The recombination rate of the charge carriers on the surface of the optimized nanocomposite is reduced significantly, resulting in superior PCA under light irradiation [45]. Electrons and holes are scattered in opposite directions, that is, electrons (e<sup>−</sup>) migrate from the CB of the heterojunction (Zn–O–Cu) to the CB of SnS, while holes (h<sup>+</sup>) move in the opposite direction [46]. These actions on the photogenerated charge carriers on the surface of the photocatalyst lead to the formation of an electric field in the region of the Zn–O–Cu/SnS heterojunction. The novel heterojunction in the nanocomposite also achieves a lower recombination rate of photogenerated charge carriers, a change in the energy bandgap, and a high light absorption capacity [47]. These properties tend to maximize the dye degradation in water bodies under solar light illumination. The achievement of maximum charge separation is advantageous for obtaining a robust photocatalytic degradation of MB. The proposed transport mechanism reactions for the separation of photogenerated charge carriers are as follows [48]:



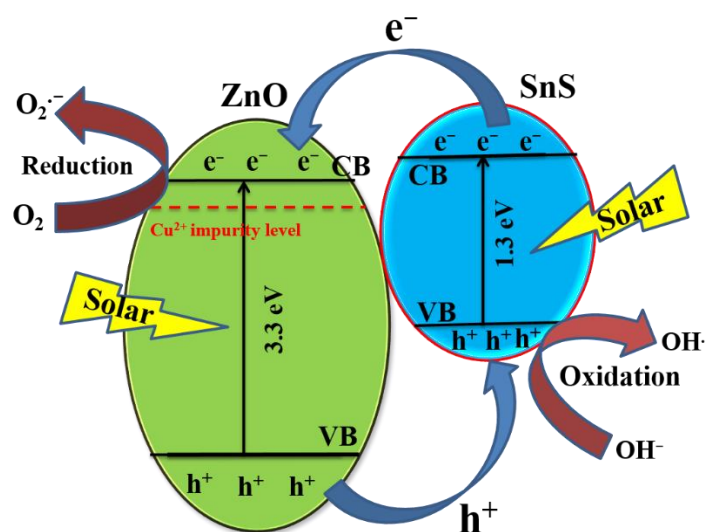


**Figure 6.** Photodegradation mechanism of MB dye using  $\text{Cu}^{2+}$ -doped ZnO–SnS nanocomposites.

The results suggest that the plasmonic effect of the heterojunction (ZS) with  $\text{Cu}^{2+}$  metal ions may help the growth of strong oxidative free radicals on the surface of the photocatalyst, which significantly improves the performance of photocatalytic degradation by  $\text{Cu}^{2+}$ -doped ZnO–SnS nanocomposites under solar light irradiation.

### 3. Materials and Methods

#### 3.1. Materials

For the fabrication of  $\text{Cu}^{2+}$ -doped ZnO–SnS nanocomposites,  $\text{Zn}(\text{CH}_3\text{COO})_2 \cdot 2\text{H}_2\text{O}$  (99.99%), NaOH (>97%),  $\text{SnCl}_4 \cdot 5\text{H}_2\text{O}$  (99.99%),  $\text{Na}_2\text{S}$  (>98%), and  $\text{Cu}(\text{NO}_3)_2$  (99.99%) precursors of analytical grade were used.

#### 3.2. Synthesis of $\text{Cu}^{2+}$ -Doped ZnO–SnS Nanocomposite

The ZnO–SnS nanocomposites were synthesized by a hydrothermal technique using the following steps: (1) 2.2 g (0.2 mol%) of  $\text{Zn}(\text{CH}_3\text{COO})_2 \cdot 2\text{H}_2\text{O}$  in 50 mL of a deionized water-ethanol mixture (1:1 ratio) and equimolar NaOH in another deionized water-ethanol mixture were mixed drop by drop; (2) 50 mL of the deionized water-ethanol mixture of  $\text{SnCl}_4 \cdot 5\text{H}_2\text{O}$  and an equal molar amount of  $\text{Na}_2\text{S}$  were added to (1); (3) 0.01 mol% of  $\text{Cu}(\text{NO}_3)_2$  in 20 mL of the water-ethanol mixture was also added to (1), which was then stirred continuously for 3–4 h, before washing with deionized water and ethanol several times to extract impurities; (4) the resulting solution was poured into a Teflon-coated high-vapor-pressure autoclave and then placed in a high-temperature muffle furnace maintained at 220 °C for 10 h; (5) the solution was centrifuged at 5000 rpm for 15 min. The sediment material was collected and dried for 4 h in a hot-air oven at 100 °C and then ground finely until powder nanoparticles were obtained. Different concentrations of  $\text{Cu}^{2+}$ -doped ZnO–SnS nanocomposites were prepared by varying the mole percentage of the Cu content (1%, 3%, and 5%) in optimized (1:0.75) ZnO–SnS (“Z–S”) samples [47]. In this paper, the synthesized samples are denoted ZS-C1, ZS-C3, and ZS-C5, respectively, while the undoped sample is denoted ZS.

#### 3.3. Characterization Techniques

Powder X-ray diffraction (XRD) data were obtained using an XPert Pro PANalytical diffractometer (Malvern, UK) with  $\text{Cu-K}\alpha$  radiation ( $\lambda = 0.15406$  nm). Transmission electron microscope (TEM) micrographs were obtained using a HITACHI H-7650 instrument (Tokyo, Japan) with an accelerating voltage of 100 kV. Powder samples were dispersed in an ethanol solution, and a drop of the homogeneous dispersion was then loaded onto a carbon-coated copper grid and allowed to dry before TEM analysis. A Thermo Scientific K-alpha

(Waltham, MA, USA) surface analysis instrument was used for XPS analysis to determine the oxidation states of the constituent elements in the sample. DRS spectra were recorded with a JASCO V-670 spectrophotometer (Tokyo, Japan) in the wavelength range of 200–900 nm to determine the energy bandgap.

#### 3.4. Photocatalytic Activity

In the present study, an aqueous solution of MB at ambient temperature was irradiated with a 150 W Abet solar simulator, and the precise output intensity over the solution was nearly one sun. The Abet solar simulator (Milford, USA) delivered the light with an intensity of 1000 W/m<sup>2</sup>. For each sample, 10 mg of prepared catalyst (Cu<sup>2+</sup>-doped ZnO–SnS) was added to 100 mL of 0.03126 mM (10 ppm) MB aqueous solution. Prior to light illumination, the solution was magnetically stirred in the dark for 1 h to maintain the adsorption/desorption equilibrium between MB and the catalyst. The final solution was then irradiated with solar light. The degradation of the MB dye was analyzed using a UV-Vis-NIR spectrophotometer using 5 mL aliquots collected from the solution. Each experiment was carried out in two parts: (1) normal conditions without a catalyst (only MB) and (2) with catalyst material (ZS-C). The photocatalytic degradation efficiency was evaluated using the formula:

$$\text{Degradation efficiency (\%)} = (1 - C/C_0) \times 100\% \quad (6)$$

where  $C_0$  is the initial concentration of MB, and  $C$  is the concentration after irradiation.

#### 4. Conclusions

In summary, Cu<sup>2+</sup>-doped ZnO–SnS nanocomposites were synthesized by a facile hydrothermal method at 220 °C for solar-light-driven photocatalysis. A mixed-phase abundance of hexagonal wurtzite ZnO and orthorhombic SnS was observed. No peaks relevant to the doping content were found. The crystallite size of the optimized nanocomposite was found to be 6.8 nm. The TEM micrographs revealed the deposition of SnS nanoparticles on the surface of the ZnO nanoflakes, and a trend of agglomeration was observed with an increase in doping concentration. The XPS analysis determined the chemical state of the constituent elements such as Zn<sup>2+</sup>, O<sup>2-</sup>, Sn<sup>2+</sup>, S<sup>2-</sup> and the successful incorporation of Cu<sup>2+</sup> ions into the ZS nanocomposite. Optical absorption spectra confirmed that the bandgap of the synthesized nanocomposites decreased with an increasing dopant content. Enhanced photocatalytic activity against the MB dye was observed under solar light illumination. The achieved degradation efficiency was 97.2% in 120 min. The enhanced photocatalytic performance of the optimal sample was attributed to the maximum separation of photoinduced charge carriers and to the formation of a heterojunction at the interface.

**Author Contributions:** Conceptualization, methodology, and writing-original draft preparation: G.D.; formal analysis, original draft preparation and review: T.R.G.; supervision and review: P.S.R.M.; formal analysis, original draft preparation and review: B.B.; supervision and review: K.Y. All authors have read and agreed to the published version of the manuscript.

**Funding:** This work was funded by the National Research Foundation of Korea (NRF) grant funded by the Korea government (MSIT) (No.2021R1C1C1011089).

**Data Availability Statement:** Not applicable.

**Acknowledgments:** The authors (Govinda Dharmana, Thirumala Rao Gurugubelli, and M.P. Srinivasa Rao) wish to express their gratitude to the GMRICT management for providing financial assistance through the SEED grant for the research.

**Conflicts of Interest:** The authors have no conflict of interest to declare that are relevant to the content of this article.

## References

1. Sarma, G.K.; Khan, A.; El-Toni, A.M.; Rashid, M.H. Shape-tunable CuO-Nd(OH)<sub>3</sub> nanocomposites with excellent adsorption capacity in organic dye removal and regeneration of spent adsorbent to reduce secondary waste. *J. Hazard. Mater.* **2019**, *380*, 120838. [[CrossRef](#)] [[PubMed](#)]
2. Aziz, K.H.H.; Miessner, H.; Mueller, S.; Mahyar, A.; Kalass, D.; Moeller, D.; Khorshid, I.; Rashid, M.A.M. Comparative study on 2,4-dichlorophenoxyacetic acid and 2,4-dichlorophenol removal from aqueous solutions via ozonation, photocatalysis and non-thermal plasma using a planar falling film reactor. *J. Hazard. Mater.* **2018**, *343*, 107. [[CrossRef](#)]
3. Chowdhury, R.; Khan, A.; Rashid, M.H. Green synthesis of CuO nanoparticles using Lantana camara flower extract and their potential catalytic activity towards the aza-Michael reaction. *RSC Adv.* **2020**, *10*, 14374. [[CrossRef](#)]
4. Narayanan, N.; Deepak, N.K. Enhancement of visible luminescence and photocatalytic activity of ZnO thin films via Cu doping. *Optik* **2018**, *158*, 1313. [[CrossRef](#)]
5. Aziz, K.H.H.; Mahyar, A.; Miessner, H.; Mueller, S.; Kalass, D.; Moeller, D.; Khorshid, I.; Rashid, M.A.M. Application of a planar falling film reactor for decomposition and mineralization of methylene blue in the aqueous media via ozonation, Fenton, photocatalysis and non-thermal plasma: A comparative study. *Process. Saf. Environ. Prot.* **2018**, *113*, 319. [[CrossRef](#)]
6. Reddy, C.V.; Reddy, K.R.; Shetti, N.P.; Shim, J.; Aminabhavi, T.M. Hetero-nanostructured metal oxide-based hybrid photocatalysts for enhanced photoelectrochemical water splitting—A review. *Int. J. Hydrogen Energy* **2020**, *45*, 18331. [[CrossRef](#)]
7. Xu, J.; Gao, Q.; Bai, X.; Zhou, P.; Wang, Y. Enhanced visible-light-induced photocatalytic degradation and disinfection activities of oxidized porous g-C<sub>3</sub>N<sub>4</sub> by loading Ag nanoparticles. *Catal. Today* **2019**, *332*, 227. [[CrossRef](#)]
8. Koutavarapu, R.; Babu, B.; Reddy, C.V.; Reddy, I.N.; Reddy, K.R.; Rao, M.C.; Aminabhavi, T.M.; Cho, M.; Kim, D.; Shim, J. ZnO nanosheets-decorated Bi<sub>2</sub>WO<sub>6</sub> nanolayers as efficient photocatalysts for the removal of toxic environmental pollutants and photoelectrochemical solar water oxidation. *J. Environ. Manag.* **2020**, *265*, 110504. [[CrossRef](#)] [[PubMed](#)]
9. Karthik, K.V.; Reddy, C.V.; Reddy, K.R.; Ravishankar, R.; Sanjeev, G.; Kulkarni, R.V.; Shetti, N.P.; Raghu, A.V. Barium titanate nanostructures for photocatalytic hydrogen generation and photodegradation of chemical pollutants. *J. Mater. Sci. Mater. Electron.* **2019**, *30*, 20646. [[CrossRef](#)]
10. Tripathi, A.M.; Mitra, S. Tin sulfide (SnS) nanorods: Structural, optical and lithium storage property study. *RSC Adv.* **2014**, *4*, 10358. [[CrossRef](#)]
11. Jayswal, S.; Moirangthem, R.S. Construction of solar spectrum active SnS/ZnO p-n heterojunction as highly efficient photocatalyst: An effect of sensitization process on its performance. *New J. Chem.* **2018**, *42*, 13689. [[CrossRef](#)]
12. Riaz, U.; Ashraf, S.M.; Kashyap, J. Role of Conducting Polymers in Enhancing TiO<sub>2</sub>-based Photocatalytic Dye Degradation: A Short Review. *Polym. Plast. Technol. Eng.* **2015**, *54*, 1850. [[CrossRef](#)]
13. Colón, G.; Maicu, M.; Hidalgo, M.C.; Navío, J.A. Cu-doped TiO<sub>2</sub> systems with improved photocatalytic activity. *Appl. Catal. B Environ.* **2006**, *67*, 41. [[CrossRef](#)]
14. Wang, H.; Yu, J.; Zhan, X.; Chen, L.; Sun, Y.; Shi, H. Direct 2D/2D Z-scheme SnNb<sub>2</sub>O<sub>6</sub>/ZnO hybrid photocatalyst with enhanced interfacial charge separation and high efficiency for pollutants degradation. *Appl. Surf. Sci.* **2020**, *528*, 146938. [[CrossRef](#)]
15. Xu, L.; Xian, F.; Zhang, Y.; Wang, W.; Qiu, K.; Xu, J. Synthesis of ZnO-decorated SnO<sub>2</sub> nanopowder with enhanced photocatalytic performance. *Optik* **2019**, *194*, 162965. [[CrossRef](#)]
16. Xu, M.; Jia, S.; Chen, C.; Zhang, Z.; Yan, J.; Guo, Y.; Zhang, Y.; Zhao, W.; Yun, J.; Wang, Y. Microwave-assisted hydrothermal synthesis of SnO<sub>2</sub>@ZnO hierarchical nanostructures enhanced photocatalytic performance under visible light irradiation. *Mater. Res. Bull.* **2018**, *106*, 74. [[CrossRef](#)]
17. Gurugubelli, T.R.; Ravikumar, R.V.S.S.N.; Koutavarapu, R. Enhanced Photocatalytic Activity of ZnO-CdS Composite Nanostructures towards the Degradation of Rhodamine B under Solar Light. *Catalysts* **2022**, *12*, 84. [[CrossRef](#)]
18. Makama, A.B.; Salmiaton, A.; Saion, E.B.; Choong, T.S.Y.; Abdullah, N. Microwave-Assisted Synthesis of Porous ZnO/SnS<sub>2</sub> Heterojunction and Its Enhanced Photoactivity for Water Purification. *J. Nanomater.* **2015**, *2015*, 108297. [[CrossRef](#)]
19. Zhang, Z.; Yi, J.B.; Ding, J.; Wong, L.M.; Seng, H.L.; Wang, S.J.; Tao, J.G.; Li, G.P.; Xing, G.Z.; Sum, T.C.; et al. Cu-Doped ZnO Nanoneedles and Nanonails: Morphological Evolution and Physical Properties. *J. Phys. Chem. C* **2008**, *112*, 9579. [[CrossRef](#)]
20. Alatawi, N.M.; Ben Saad, L.; Soltane, L.; Moulahi, A.; Mjejri, I.; Sediri, F. Enhanced solar photocatalytic performance of Cu-doped nanosized ZnO. *Polyhedron* **2021**, *197*, 115022. [[CrossRef](#)]
21. Karthik, K.V.; Raghu, A.V.; Reddy, K.R.; Ravishankar, R.; Sangeeta, M.; Shetti, N.P.; Reddy, C.V. Green synthesis of Cu-doped ZnO nanoparticles and its application for the photocatalytic degradation of hazardous organic pollutants. *Chemosphere* **2022**, *287*, 132081. [[CrossRef](#)] [[PubMed](#)]
22. Rao, G.T.; Ravikumar, R.V.S.S.N. Novel Fe-doped ZnO-CdS nanocomposite with enhanced visible light-driven photocatalytic performance. *Mater. Res. Innov.* **2020**, *25*, 215. [[CrossRef](#)]
23. Patterson, A.L. The Scherrer Formula for X-Ray Particle Size Determination. *Phys. Rev.* **1939**, *56*, 978. [[CrossRef](#)]
24. Thirumala Rao, G.; Babu, B.; Joyce Stella, R.; Pushpa Manjari, V.; Ravikumar, R.V.S.S.N. Spectral investigations on undoped and Cu<sup>2+</sup>-doped ZnO-CdS composite nanopowders. *Spectrochim. Acta A* **2015**, *139*, 86. [[CrossRef](#)] [[PubMed](#)]
25. Hanh, N.T.; Tri, N.L.M.; Thuan, D.V.; Tung, M.H.T.; Pham, T.D.; Minh, T.D.; Trang, H.T.; Binh, M.T.; Nguyen, M.V. Monocrotophos pesticide effectively removed by novel visible light driven Cu doped ZnO photocatalyst. *J. Photochem. Photobiol. A* **2019**, *382*, 111923. [[CrossRef](#)]

26. Maryam, M.A.; Masoud, S.N. Metal (Mn, Co, Ni and Cu) doped ZnO-Zn<sub>2</sub>SnO<sub>4</sub>-SnO<sub>2</sub> nanocomposites: Green sol-gel synthesis, characterization and photocatalytic activity. *J. Mol. Liq.* **2017**, *248*, 197.
27. Liu, Y.; Zhou, Y.; Zhou, X.; Jin, X.; Li, B.; Liu, J.; Chen, G. Cu doped SnS<sub>2</sub> nanostructure induced sulfur vacancy towards boosted photocatalytic hydrogen evolution. *Chem. Eng. J.* **2021**, *407*, 127180. [[CrossRef](#)]
28. Sajid, M.M.; Shad, N.A.; Javed, Y.; Khan, S.B.; Zhang, Z.; Amin, N.; Zhai, H. Preparation and characterization of Vanadium pentoxide (V<sub>2</sub>O<sub>5</sub>) for photocatalytic degradation of monoazo and diazo dyes. *Surf. Interfaces* **2020**, *19*, 100502. [[CrossRef](#)]
29. Jia, T.; Fu, F.; Li, J.; Deng, Z.; Long, F.; Yu, D.; Cui, Q.; Wang, W. Rational construction of direct Z-scheme SnS/g-C<sub>3</sub>N<sub>4</sub> hybrid photocatalyst for significant enhancement of visible-light photocatalytic activity. *Appl. Surf. Sci.* **2020**, *499*, 143941. [[CrossRef](#)]
30. Zhang, Q.X.; Ma, S.Y.; Zhang, R.; Tie, Y.; Pei, S.T. Optimization ethanol detection performance manifested by SnS/SnS<sub>2</sub> nanoparticles. *Mater. Lett.* **2020**, *258*, 126783. [[CrossRef](#)]
31. Tang, R.; Su, H.; Sun, Y.; Zhang, X.; Li, L.; Liu, C.; Zeng, S.; Sun, D. Enhanced photocatalytic performance in Bi<sub>2</sub>WO<sub>6</sub>/SnS heterostructures: Facile synthesis, influencing factors and mechanism of the photocatalytic process. *J. Colloid Interface Sci.* **2016**, *466*, 388. [[CrossRef](#)] [[PubMed](#)]
32. Jubu, P.R.; Yam, F.K.; Igba, V.M.; Beh, K.P. Tauc-plot scale and extrapolation effect on bandgap estimation from UV-vis-NIR data—A case study of β-Ga<sub>2</sub>O<sub>3</sub>. *J. Solid State Chem.* **2020**, *290*, 121576. [[CrossRef](#)]
33. Zhou, J.; Zhang, Z.; Kong, X.; He, F.; Zhao, R.; Wu, R.; Wei, T.; Wang, L.; Feng, J. A novel P-N heterojunction with staggered energy level based on ZnFe<sub>2</sub>O<sub>4</sub> decorating SnS<sub>2</sub> nanosheet for efficient photocatalytic degradation. *Appl. Surf. Sci.* **2020**, *510*, 145442. [[CrossRef](#)]
34. Khanchandani, S.; Kundu, S.; Patra, A.; Ganguli, A.K. Band Gap Tuning of ZnO/In<sub>2</sub>S<sub>3</sub> Core/Shell Nanorod Arrays for Enhanced Visible-Light-Driven Photocatalysis. *J. Phys. Chem. C* **2013**, *117*, 5558. [[CrossRef](#)]
35. Ahmad, M.; Ahmed, E.; Hong, Z.L.; Khalid, N.R.; Ahmed, W.; Elhissi, A. Graphene-Ag/ZnO nanocomposites as high performance photocatalysts under visible light irradiation. *J. Alloys Compd.* **2013**, *577*, 717. [[CrossRef](#)]
36. Munawar, T.; Iqbal, F.; Yasmeen, S.; Mahmood, K.; Hussain, A. Multi metal oxide NiO-CdO-ZnO nanocomposite-synthesis, structural, optical, electrical properties and enhanced sunlight driven photocatalytic activity. *Ceram. Int.* **2020**, *46*, 2421. [[CrossRef](#)]
37. Tao, Y.M.; Ma, S.Y.; Chen, H.X.; Meng, J.X.; Hou, L.L.; Jia, Y.F.; Shang, X.R. Effect of the oxygen partial pressure on the microstructure and optical properties of ZnO:Cu films. *Vacuum* **2011**, *85*, 744. [[CrossRef](#)]
38. Saravanan, R.; Sacari, E.; Gracia, F.; Khan, M.M.; Moquera, E.; Gupta, V.K. Conducting PANI stimulated ZnO system for visible light photocatalytic degradation of coloured dyes. *J. Mol. Liq.* **2016**, *221*, 1029. [[CrossRef](#)]
39. Abdiryim, T.; Ali, A.; Jamal, R.; Sman, Y.; Zhang, Y. A facile solid-state heating method for preparation of poly(3,4-ethelenedioxythiophene)/ZnO nanocomposite and photocatalytic activity. *Nanoscale Res. Lett.* **2014**, *9*, 89. [[CrossRef](#)]
40. Krishnan, A.; Vishawanathan, P.V.; Mohan, A.C.; Panchami, R.; Viswanath, S.; Krishnan, A.V. Tuning of Photocatalytic Performance of CeO<sub>2</sub>-Fe<sub>2</sub>O<sub>3</sub> Composite by Sn-doping for the Effective Degradation of Methylene Blue (MB) and Methyl Orange (MO) dyes. *Surf. Interfaces* **2021**, *22*, 100808. [[CrossRef](#)]
41. Ameen, S.; Akhtar, M.S.; Kim, Y.S.; Yang, O.B.; Shin, H.S. An effective nanocomposite of polyaniline and ZnO: Preparation, characterizations, and its photocatalytic activity. *Colloid Polym. Sci.* **2011**, *289*, 415. [[CrossRef](#)]
42. Banumathi, S.; Uma, J.; Ravi, A.; Balaraj, B.; Siva, C.; Illanchezhian, P.; Kumar, G.M. Rapid sun-light driven photocatalytic functions of 3D rGO/ZnO/Ag heterostructures via improved charge transfer kinetics. *J. Mater. Res. Technol.* **2021**, *10*, 1301. [[CrossRef](#)]
43. Eskizeybek, V.; Sari, F.; Giilce, H.; Avci, A. Preparation of the new polyaniline/ZnO nanocomposite and its photocatalytic activity for degradation of methylene blue and malachite green dyes under UV and natural sun lights irradiations. *Appl. Catal. B* **2012**, *119–120*, 197. [[CrossRef](#)]
44. Shavisi, Y.; Sharifnia, S.; Mohamadi, Z. Solar-light-harvesting degradation of aqueous ammonia by CuO/ZnO immobilized on pottery plate: Linear kinetic modeling for adsorption and photocatalysis process. *J. Environ. Chem. Eng.* **2016**, *4*, 2736. [[CrossRef](#)]
45. Makama, A.B.; Salmiation, A.; Saion, E.B.; Choong, T.S.Y.; Abdullah, N. Microwave Assisted Synthesis of Porous ZnO/SnS Heterojunction and its Application in Visible Light Degradation of Ciprofloxacin. *AIP Conf. Proc.* **2016**, *020018*, 1733.
46. Wang, L.; Zhai, H.; Jin, G.; Li, X.; Dong, C.; Zhang, H.; Yang, B.; Xie, H.; Sun, H. 3D porous ZnO-SnS p-n heterojunction for visible light driven photocatalysis. *Phys. Chem. Chem. Phys.* **2017**, *19*, 16576–16585. [[CrossRef](#)] [[PubMed](#)]
47. Govinda, D.; Rao, M.P.S.; Murthy, P.D. Enhanced photocatalytic activity in hydro-thermally grown nano structured ZnO/SnS core-shell composites. *Z. Nat. A* **2022**, *77*, 153–169.
48. Altaf, S.; Ajaz, H.; Imran, M.; Ul-Hamid, A.; Naz, M.; Aqeel, M.; Shahzadi, A.; Shahbaz, A.; Ikram, M. Synthesis and characterization of binary selenides of transition metals to investigate its photocatalytic, antimicrobial and anticancer efficacy. *Appl. Nanosci.* **2020**, *10*, 2113–2127. [[CrossRef](#)]